https://doi.org/10.5194/egusphere-2025-5015
Preprint. Discussion started: 23 December 2025

A State-Space Model for Monitoring Greenland Ice Sheet Surface Elevation Change from CryoSat-2

Natalia H. Andersen[1], Sebastian B. Simonsen[1], Karina Nielsen[1], Mai Winstrup[1], Baptiste Vandecrux[2], Hui Gao[3], Beata Csatho[3], Anton Schenk[3], and Louise Sandberg Sørensen[1]

[1]DTU Space, Elektrovej 328, 2800 Kgs Lyngby, Denmark
[2]Geological Survey of Denmark and Greenland, Department of Glaciology and Climate, Øster Voldgade 10, 1350 Copenhagen K, Denmark
[3]Department of Earth Sciences, University at Buffalo, 413 Hochstetter Hall, Buffalo NY 14260, United States

Correspondence: Natalia H. Andersen (Naand@dtu.dk)

Abstract. We present a data-driven State Space Model (SSM) framework, the Three-Dimensional Elevation Change Model (3D-ECM), for deriving monthly surface elevation changes of the Greenland Ice Sheet from CryoSat-2 radar altimetry. Unlike approaches with pre-defined seasonal models, seasonality here emerges directly from the data, enabling the detection of seasonal cycles, long-term trends, and abrupt changes. The method combines a Gaussian Markov Random Field for spatial dependence with an autoregressive process for temporal correlations, allowing robust signal extraction even in regions with sparse or irregular sampling. With this framework, we derive monthly elevation changes for the Greenland ice sheet in 5 km resolution over the period 2011-2025.

Validation against independent datasets shows strong agreement: correlations between our surface elevation change (dSEC) and surface elevation records from Automatic Weather Stations range from 0.58 to 0.75, with the highest agreement at the AWS station named KAN_M, while comparisons with time series derived from a fusion between laser altimetry-based data and a firn densification model yield r values up to 0.76. Additional comparisons with ICESat-2 and NASA Operation IceBridge airborne data confirm that spatio-temporal smoothing of the dSEC reduces standard deviation by 40–45$\%$ while maintaining minimal bias.

The resulting dSEC dataset provides high-resolution, temporally consistent elevation change records that capture both seasonal variability and long-term trends of the Greenland Ice Sheet. The flexible and fully data-driven 3D-ECM framework is directly transferable to other altimetry missions and multi-sensor records, offering a pathway toward continuous, long-term monitoring of ice-sheet elevation change across satellite generations.

1 Introduction

The Arctic has been warming at up to four times the global average since 1979 (Rantanen et al., 2022; Chylek et al., 2022; Sweeney et al., 2023). This rapid atmospheric warming has accelerated the mass loss from the Greenland Ice Sheet (GrIS) over the last decades (Khan et al., 2022; Løkkegaard et al., 2024), making it a significant contributor to global sea-level rise (Moon

https://doi.org/10.5194/egusphere-2025-5015
Preprint. Discussion started: 23 December 2025

et al., 2018; Mouginot et al., 2019; Box et al., 2022; Khan et al., 2022). Rising sea levels will impact coastal communities worldwide in the coming decades (Bamber et al., 2010; Gardner et al., 2013; Forsberg et al., 2017; Otosaka et al., 2023).

Accurate and timely data on ice sheet dynamics are therefore essential for understanding the processes driving mass loss and refining projections of future sea-level rise (Williams et al., 2021). Satellite radar altimetry has emerged as a powerful technique for monitoring ice sheet Surface Elevation Change (SEC), which, under certain assumptions, can be converted into estimates of ice sheet mass loss and sea-level contribution (Simonsen et al., 2021). ESA's CryoSat-2, carrying the SAR Interferometric Radar Altimeter (SIRAL) (Wingham et al., 2006), was specifically designed to measure SEC in ice-covered regions, regardless of cloud cover or solar illumination, making it particularly valuable for the polar regions. With more than a decade of continuous observations, CryoSat-2 provides an unprecedented record for assessing both long-term trends and shorter-term variability in GrIS SEC (Lai and Wang, 2022; Ravinder et al., 2024).

Capturing seasonal fluctuations and short-term events, such as glacier calving or enhanced meltwater runoff, requires a higher temporal resolution than the annual SEC products traditionally derived from radar altimetry. Conventional approaches, such as the plane-fit algorithm (Simonsen et al., 2017; Sørensen et al., 2018), extract a mean SEC over a multi-year period, but this limits their ability to resolve seasonal fluctuations and short-term events. As a result, much of the seasonal signal and many episodic anomalies remain hidden in aggregated annual products. To address this, new processing methods have been developed to derive monthly SEC from radar altimetry (Lai and Wang, 2022; Zhang et al., 2022; Ravinder et al., 2024; Nilsson et al., 2024; Khan et al., 2025). These efforts mark a major step forward as they provide a finer temporal detail, which enables a better integration with regional climate models and in situ observations.

Here, we propose the integration of state-space models (SSMs) with radar altimetry to be a promising avenue to detect subtle patterns in surface elevation changes that may be overlooked by existing methods. SSMs have already demonstrated their potential in related Earth Observation applications, for example, in deriving temporally densified water level time series for a river based on multi-mission satellite altimetry (Nielsen et al., 2022). This flexible and data-driven SSM framework can be applied across satellite altimetry missions to generate continuous, gap-filled SEC time series, with seasonal signals emerging directly from the data rather than from predefined models such as in previous studies by e.g. Sørensen et al. (2018) or Khan et al. (2025). In addition, SSMs explicitly separate signal from noise, and are able to handle irregular or missing data, and may provide coherent uncertainty estimates while accounting for spatial and temporal dependencies (Kristensen et al., 2016). Extending this methodology to ice sheets provides a powerful means to generate continuous, gap-filled time series of SEC across a range of spatial and temporal scales, independent of the specific satellite mission.

In this study, we develop our model 3D-ECM to derive surface elevation change (dSEC) over the entire Greenland Ice Sheet from CryoSat-2 radar altimetry, where the prefix "d" denotes that the model can be configured to any desired temporal resolution; here it is applied at monthly intervals. The derived dataset contains monthly surface-elevation-change estimates that reflect both multi-year trends and intra-annual variations derived from the state-space model.

2 Data sets

The construction of the dSEC data product is based on CryoSat-2 altimetry data and is validated against independent datasets from ICESat-2, Operation IceBridge (OIB), Automatic Weather Stations (AWS), and laser altimetry-based SERAC (Surface Elevation Reconstruction And Change detection) time series fusion, incorporating firn height change estimation.

2.1 Cryosat-2 data

CryoSat-2 is a radar altimetry satellite mission developed by the European Space Agency (ESA) to monitor changes in the cryosphere. The SIRAL radar onboard CryoSat-2 operates at Ku band (13.5 GHz). Over the ice sheet margins, it leverages its two antennas to provide synthetic aperture radar interferometric (SARIn) mode, while it only collects single-pulse, nadir-looking data in low-resolution mode (LRM) over the ice sheet interior (Bouzinac, 2022).

In this study, we use Point Of Closest Approach (POCA) elevations available from CryoSat-2 Level-2 SARIn and LRM data products from baseline E (Bouzinac, 2022) as the primary input for estimating monthly dSEC over the Greenland Ice Sheet. POCA elevations theoretically represent the point on the ground closest to the radar beam direction, where the strongest radar return is assumed to originate. The Level-2 data include geophysical corrections such as ionospheric delay, wet and dry tropospheric path delays, solid Earth and ocean tides, and surface scattering corrections. In LRM mode, the SIRAL pulse-limited footprint covers approximately 2.15 km^2, with an effective diameter of about 1.65 km. In SAR/SARIn mode, the across-track pulse-limited footprint is similarly 1.65 km, while the along-track beam-limited footprint is approximately 305 m (yielding an effective along-track resolution of 400 m), resulting in a total Doppler-limited illuminated area of 0.5 km^2 (Bouzinac, 2022).

2.2 ICESat-2 validation data

To validate the dSEC derived from CryoSat-2, we use data from NASA's ICESat-2 mission, which provides high-resolution laser altimetry observations over the GrIS. Specifically, we use the ATL15 gridded SEC product (Smith et al., 2022), which is derived from the annual ATL11 height product.

We use ATL15 lag-8 data, which correspond to 24-month SEC estimates centered around each observation month. This lag setting provides a balance between temporal resolution and spatial coverage, allowing a meaningful comparison of the long-term trend with our monthly gridded dSEC product derived from CryoSat-2.

2.3 Operation IceBridge Validation Data

To complement the satellite dataset, we also validate against data from NASA's OIB mission, which provides airborne laser altimetry measurements over the polar regions from 2009 to 2019 (Studinger, 2023). OIB was designed to bridge the observational gap between the ICESat and ICESat-2 missions, providing detailed measurements of ice sheet topography with high spatial resolution and accuracy.

https://doi.org/10.5194/egusphere-2025-5015
Preprint. Discussion started: 23 December 2025

Here, we use OIB Level-4 gridded SEC products, which are derived from repeated airborne laser altimetry tracks (Studinger, 2023). These datasets give SEC estimates computed over selected multi-year intervals and are provided on a spatial grid.

We use data from the OIB campaigns between 2011 and 2016 over the Greenland Ice Sheet, focusing on regions that spatially overlap with our CryoSat-2 dSEC coverage.

2.4 Seasonal surface height change from accumulation and ablation at Automatic Weather Stations

The seasonal amplitudes in our dSEC product are evaluated with data from the Programme for Monitoring of the Greenland Ice Sheet (PROMICE) (Ahlstrøm et al. , 2008) and the Greenland Climate Network (GC-Net) AWS (Fausto et al., 2021; Vandecrux et al., 2024). AWS sites are divided between accumulation sites, where snow accumulated in winter does not melt away in the summer, and ablation sites, where the winter snow melts away and is followed by melting of the glacial ice. At accumulation sites, the AWS cannot capture the surface height change stemming from firn compaction below the station's anchoring depth.

A near-continuous record of surface height relative to the AWS's installation height is derived by merging data from multiple instruments (Vandecrux et al., 2024) (variable: z_surf_combined). At ablation sites, it combines data from a station-mounted sonic ranger, a stake-mounted sonic ranger, and a borehole pressure transducer. During ablation periods, the pressure transducer (or, if failing, the stake-mounted sonic ranger) defines surface height, while winter values are based on the adjusted average of both sonic ranger heights. The record is manually corrected for shifts that may occur during maintenance.

These AWS surface heights are not absolute heights, as they are referenced to the installation height and hence only represent the accumulation and ablation that occur at the ice sheet surface. They do not include bedrock-related motion, which contributes 1-2 cm uplift every year (Liu et al., 2017) , nor thinning or thickening of the ice below, which may contribute to surface height changes of the same order of magnitude as changes caused by surface melt (Bevan et al., 2015; Kehrl et al., 2017). Yet, in the absence of Greenland-wide, temporally resolved maps of thinning/thickening due to ice dynamics, the AWS-derived surface heights provide a lower bound to the summertime thinning and to the wintertime thickening.

We use AWS data from the melt periods to evaluate the seasonal amplitude in the dSEC data product at the following three locations: Stations KAN_M and JAR (West Greenland), and KPC_U (North Greenland) (See Figure 1 and in Table 1). These stations were selected because they are located away from the edges of the dSEC grid, ensuring a more reliable comparison with the dSEC data product.

2.5 Surface elevation change time series from laser altimetry-based SERAC and SERAC-FDM fusion

To further evaluate the seasonal amplitude of the dSEC data product, we compare it with the SERAC elevation change time series (Schenk and Csatho , 2012; Csatho et al., 2014; Schenk et al., 2014). The SERAC time series are constructed for the locations of the three AWS stations (Table 1).

The SERAC timeseries is constructed based on a 10-day surface elevation change time series derived from fusing laser altimetry-based surface elevation change time series with firn height change estimations. First the irregularly sampled surface elevation change time series are reconstructed using the SERAC method. The SERAC time series is based on data from all NASA's airborne and satellite laser altimetry missions and includes observations from the Airborne Topographic Mapping

Table 1. Coordinates of the four AWS stations and their corresponding SERAC sites.

Station	AWS		SERAC ID	SERAC	
	Lon (°E)	Lat (°N)		Lon (°E)	Lat (°N)
KAN_M	-48.816526	67.065729	3001210	-48.991299	66.982621
JAR	-49.682014	69.498584	6002099	-49.699051	69.391009
KPC_U	-25.170450	79.833907	28000270	-26.024806	79.792897

system (ATM), the Land, Vegetation, and Ice Sensor (LVIS) airborne sensors (MacGregor et al., 2021), the Ice Cloud and land Elevation (ICESat, Zwally et al., 2002) and ICESat-2 satellites (Markus et al., 2017). SERAC reconstructs the time series of surface elevation change by simultaneously fitting 1 km^2 polynomial surface patches and modeling the elevation change at their centroids using all the laser altimetry measurements within the surface patches. The locations of the time series are primarily determined by ICESat ground track crossovers and ICESat's overlaps with ATM or LVIS to obtain long-term elevation change. Over the Greenland Ice Sheet, SERAC provides over 54,000 time series with irregular temporal sampling determined by the spatiotemporal distribution of the laser altimetry data.

The 10-day resolution surface elevation change time series is calculated as follows. We removed the Glacial Isostatic Adjustment (GIA) uplift rate (Adhikari et al. , 2021; Milne et al., 2018) and firn height change from the SERAC surface elevation change time series using the nearest neighbor in space and time to determine the ice thickness change due to ice dynamics. Firn height change, which represents the surface elevation change due to all surface processes, such as precipitation, melt, and firn compaction, is modeled by the Firn Densification Models (FDMs). We use the FDM: GEMBv1.0 (Gardner et al., 2023). We estimated the 10-day high temporal resolution time series from the relatively smooth discrete dynamic thickness change time series using the Approximation by Localized Penalized Spline (ALPS) method (Shekhar et al., 2021). By combining the interpolated dynamic thickness change time series with the GIA correction and firn height change estimations, we derived high-temporal-resolution surface elevation change time series at the location of the SERAC time series (Shekhar et al., 2021).

The seasonal elevation changes in this SERAC-FDM fusion product are well constrained by laser altimetry measurements when sampled seasonally. However, during years with few or no laser altimetry measurements, the seasonal signal is primarily determined by firn height change estimations from FDMs. In this case, seasonality can vary depending on the FDMs selected, and seasonal ice thickness changes due to, e.g., ice dynamics in tidewater glaciers may be missed.

3 State-Space Model

To model the ice surface elevation as a function of time and space, we employ our model 3D-ECM, a data-driven State-Space Model (SSM) designed to estimate monthly elevation change fields. We define a target grid of 5 km resolution in a polar stereographic projection (EPSG:3413) covering the Greenland Ice Sheet. CryoSat-2 POCA ice surface elevations are extracted

https://doi.org/10.5194/egusphere-2025-5015
Preprint. Discussion started: 23 December 2025

using the GrIS ice mask from Rignot et al. (2012), and use elevations relative to the ArcticDEM Mosaic V 4.1 (Porter et al., 2023). The model thus estimates anomalies relative to this DEM rather than absolute surface heights.

The availability of the CryoSat-2 POCA elevation anomalies varies in both space and time, highlighting the need for an approach that accounts for both spatial and temporal correlations to reconstruct a field of ice surface elevation anomalies in a novel and efficient way. This is done via a state-space approach, in which the evolution of surface height in space and time is represented as a set of hidden states that are indirectly observed through noisy satellite elevation measurements. In this framework, the hidden states correspond to the true, but unobservable, surface height anomalies on a regular grid. The observations are the CryoSat-2 Level-2 POCA elevation anomalies relative to ArcticDEM. By linking the hidden and observed components through probabilistic relationships, a State-space model provides a statistical framework that separates measurement noise from true elevation changes.

The large amount of satellite data requires a computationally efficient approach to reconstruct the spatial-temporal field of surface elevation anomalies H^{true}. To do this, we apply a Gaussian Markov Random Field (GMRF) (Rue and Held (2005)). A GMRF is a multivariate Gaussian random field in which the probability of each location is conditionally dependent only on its neighbors, leading to a sparse representation of the precision (inverse covariance) matrix. This is computationally efficient compared to a Gaussian Process (GP) model, in which each location is correlated with every other through a dense covariance matrix that requires costly matrix inversion. Instead, sparsity in the GMRF allows operations to scale almost linearly with the number of grid cells, whereas GP models typically scale cubically with data size.

To model the ice surface elevation anomalies as a function of time and space, we define a 3-dimensional regular grid. In the spatial dimension, we use a target grid with a 5 km resolution in a polar stereographic projection (EPSG:3413) covering the Greenland Ice Sheet. In the temporal dimension, a monthly resolution is selected.

Here, we assume that an observation of ice elevation anomaly H_i^{obs} is a function of space (x,y) and time t is represented by the following expression.

$$H_i^{obs}(x,y,t) = H_i^{model}(x,y,t) + \epsilon_i(x,y,t), \quad \epsilon_i \sim N(0,\sigma_{obs}^2), \tag{1}$$

where H_i^{model} is the true unobserved elevation anomaly, and ϵ_i represents the observational error, which here is assumed to be Gaussian with the standard deviation σ_{obs}. The modeled elevation anomaly is represented by a Gaussian Markov random field consisting of a spatial and temporal component with a mean and covariance given as

$$H^{model}(x,y,t) \sim N(\mu, \sigma_p^2 (Q_1 \otimes Q_2)^{-1}). \tag{2}$$

Here, Q_1 and Q_2 are the precision matrices that define the neighbor structure related to the spatial and temporal parts of the GMRF. The spatial part of the precision matrix is defined as

$$\mathbf{Q_1} = \phi \cdot \mathbf{Q_0} + I,$$

where ϕ is a model parameter controlling the spatial correlation, I is the identity matrix, and $\mathbf{Q_0}$ defines the neighborhood structure, which is described as

$$\mathbf{Q_0}(i,j) = \begin{cases} \text{number of neighbors of node } i, & \text{if } i = j, \\ -1, & \text{if } i \sim j, \\ 0, & \text{otherwise.} \end{cases}$$

In our framework, the neighborhood structure is built with a 4-nearest-neighbor structure (each grid cell connects to its north, south, east, and west neighbors). The notation $i \sim j$ indicates that the grid cells i and j share an edge (are directly adjacent to that 4-neighborhood). The precision matrix Q_2 related to the autoregressive process of order 1 is defined as

$$Q_2 = \begin{pmatrix} 1 & -\rho & & & \\ -\rho & 1+\rho^2 & \ddots & & \\ & \ddots & \ddots & \ddots & \\ & & \ddots & 1+\rho^2 & -\rho \\ & & & -\rho & 1 \end{pmatrix}$$

where ρ is a parameter that controls the temporal correlation assumed to be between -1 and 1 to ensure that the process is stationary. In summary, the full model parameters vector $\theta = (\sigma_{obs}, \sigma_p, \mu, \phi, \rho)$ and the hidden states H^{true} are estimated by the joint likelihood function

$$L(H^{obs}, H^{true}, \theta) = L(H^{obs}, \theta)L(H^{true})$$

As the hidden states H^{true} are unobserved, the joint likelihood cannot be calculated directly. Instead, we form the marginal likelihood function, which is only dependent on the fixed model parameters and the observation.

$$L_M(H^{obs}, \theta) = \int L(H^{obs}, H^{true}, \theta) dH^{true}.$$

The 3D model of ice elevation anomalies is implemented in the open source software R using the Template Model Builder (RTMB) (Kristensen et al., 2016). In RTMB, the marginal likelihood is derived via the Laplace approximation. In short, this is a second-order Taylor approximation of the logarithm of the function to be integrated around the optimum. In practice, this will change an integral into an optimization problem.

The GMRF captures both the spatial coherence and temporal evolution of elevation changes. This joint formulation allows efficient and realistic reconstruction of surface elevation change over the Greenland Ice Sheet, even in areas with irregularly distributed data. RTMB also reports the model uncertainty, which is approximated via the generalized delta-method, and the variance is expressed as

$$\mathrm{var}(\hat{H}^{true}) = H_2^{-1} + (\nabla \hat{H}^{true}(\theta))^t H_1^{-1} \nabla \hat{H}^{true}$$

Here H_2 is the block of full Hessian matrix related to the hidden states, H_1 is the Hessian matrix related to the parameters, and $\nabla \hat{H}^{true}$ are the gradients of the hidden states with respect to the models parameters θ (see e.g. Thorson and Kristensen, 2024).

To reduce unrealistic high-frequent variability and enhance the spatiotemporal coherence of the surface elevation change dataset, we apply a two-step postprocessing of the monthly dSEC gridded fields. First, each monthly elevation map is smoothed with a median spatial filter with a window size of 5 grid cells to suppress small-scale noise while retaining the larger-scale elevation signals. Secondly, for temporal consistency, a Savitzky–Golay filter (Gallagher, 2020) is applied along the time axis. For the seasonal component, we use a 17-month window, which is longer than the annual cycle and therefore provides a smoothed and damped representation of the seasonal signal while removing month-scale irregularities. To extract the multi-year trend, we use a 41-month window, which effectively isolates the long-term trends of SEC. This procedure effectively suppresses noise and outlier-driven seasonal spikes, while preserving the large-scale spatial patterns and long-term elevation-change signals. The trends of both the raw (pre-smoothing) and the smoothed dSEC grids will be evaluated separately in Section 4.1.1. The spatial and temporal postprocessing is applied only to the dSEC values, while the grid-cell uncertainties come directly from the state-space model and are not smoothed. The uncertainties therefore, represent the posterior variance estimated from the Hessian in RTMB, independent of the filtering. Spatial median filtering and temporal Savitzky-Golay smoothing reduce high-frequency noise in the dSEC fields, but they do not modify the uncertainty estimates, which remain conservative and model-based

4 Results

Using the described 3D-ECM model framework, we computed the monthly surface elevation changes across the GrIS at a 5 km resolution using radar satellite data from the CryoSat-2 L2 data product. Selected elevation change timeseries produced by our 3D-ECM are presented in Figure 1. The spatial map of average elevation change from 2011-2025 (Panel **D** in Figure 1) places these trends in context: we observe widespread thinning along the margins and generally stable or slightly thickening conditions in the interior (in the following defined as areas above 1500 m elevation based on ArcticDEM) of the ice sheet. The average trend in surface elevation change over the entire GrIS is -0.069 ± 0.002 (m/yr), as illustrated in Figure 2, whereas the trend in the ablation zone (defined as areas below 1500 m elevation based on ArcticDEM) is -0.314 ± 0.009 (m/yr). Regional uncertainties in Figure 2 were calculated by combining the grid-cell uncertainties produced by the state-space model using an area-weighted approach. For each region, the uncertainty values from all grid cells were aggregated while accounting for the size of each cell in the polar stereographic projection. Larger cells therefore contribute proportionally more to the regional estimate than smaller ones. This provides a representative regional uncertainty that reflects both the spatial distribution and the relative area of the contributing grid cells.

To assess regional variability and temporal evolution, we extracted time series from six locations (Panels A-C and E-G in Figure 1) representative of dynamically active outlet glaciers: Petermann, Nioghalvfjerdsbræ (79° N Glacier; hereafter 79N),

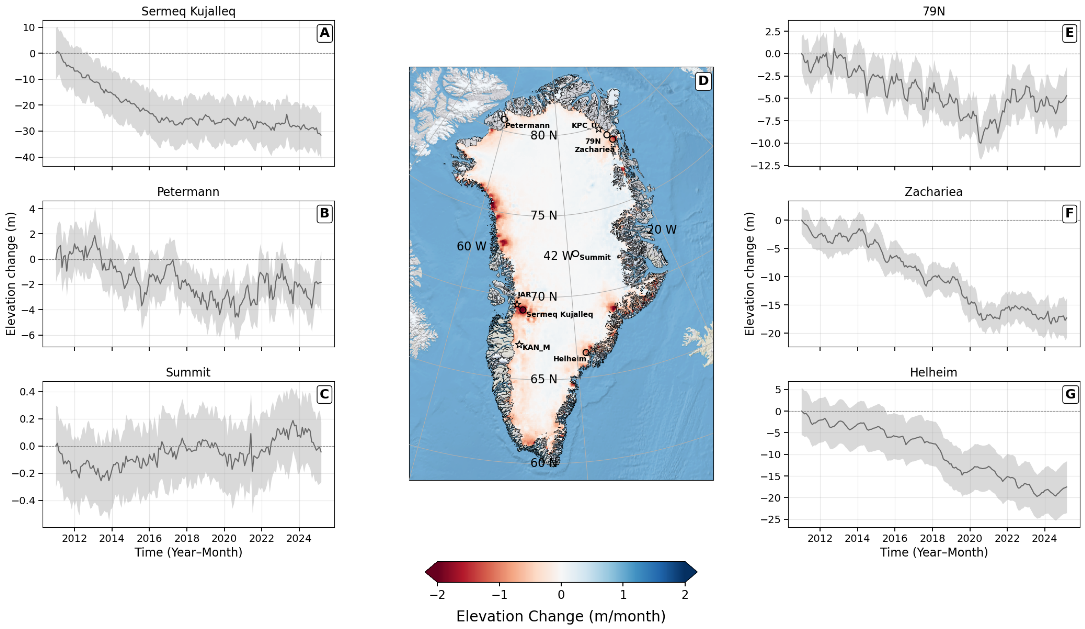

Figure 1. Time series of surface elevation change at six selected locations across the Greenland Ice Sheet from the smoothed CryoSat-2 dSEC product. Panels **A-C** and **E-G** show time series of dSEC for Sermeq Kujalleq, Petermann, Summit, 79N, Zachariae, and Helheim, respectively. Shaded envelopes in the time series panels indicate model uncertainty. Panel **D** shows the spatial distribution of elevation change rate (m month^{-1}) over 2011-2025. The four validation sites are marked on the map with yellow stars.

Zachariae, Sermeq Kujalleq, and Helheim, as well as a site representative of the relatively stable interior region at Summit Station. The time series are extracted from single grid cells, with shaded areas in Figure 1 representing 3D-ECM estimated uncertainty. Derived from the smoothed CryoSat-2 dSEC product, they reveal spatially varying elevation change patterns from 2011 to 2025. The interior site at Summit shows a modest thickening trend of 0.017 ± 0.001 (m/yr) over the 14-year period, not far from the negligible average negative trend for the entire interior ice sheet -0.014 ± 0.002 (m/yr).

All marginal sites exhibit pronounced thinning. Sermeq Kujalleq experiences the strongest thinning of -1.7 ± 0.074 (m/yr), which is above the general trend of the ablation zone trend. The maximum observed thinning at Sermeq Kujalleq occurred during the early part of the time period from 2011 to 2018.

The CryoSat-2 Level-2 altimetry data contain a spatial data gap over the fast-flowing part of Sermeq Kujalleq, where steep topography and complex radar scattering hinder reliable surface elevation retrievals, as seen in Figure 3, which provides a detailed example for the Sermeq Kujalleq, showing dSEC for three grid cells located inside and outside the persistent data gap for CryoSat-2 data. Grid cells B and C are located within the persistent CryoSat-2 data gap, while A is situated further inland in an area with higher data density. The associated uncertainties differ among the three points, reflecting the varying

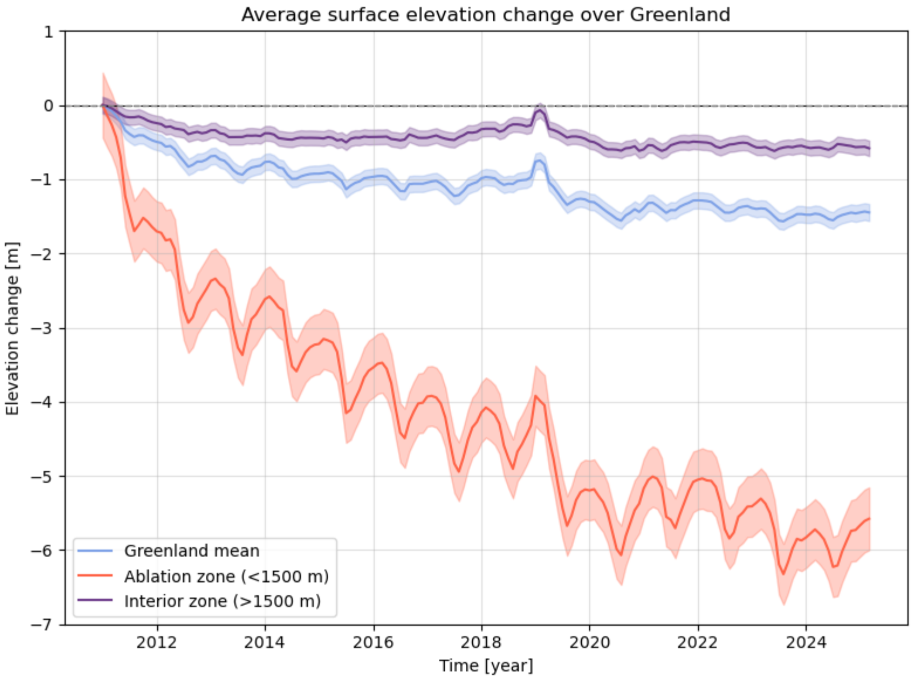

Figure 2. The average time series of surface elevation changes across the entire GrIS (in blue), the interior (here defined as areas above 1500 meters of elevation based onArcticDEM; in purple), and for the marginal zone (areas below 1500 meters of elevation; in red). Shaded envelopes indicate area-weighted uncertainties adjusted for spatial correlation.

data density, with higher uncertainties in areas of sparse CryoSat-2 coverage and lower uncertainties inland where data are more abundant. These time series reveal distinct seasonal cycles and interannual variability, demonstrating the ability of this approach to resolve fine-scale temporal changes in rapidly evolving glacier systems.

4.1 Validation and Intercomparison

To evaluate the accuracy and reliability of the CryoSat-2-derived dSEC product over the Greenland Ice Sheet, we performed a validation using both satellite and airborne datasets. The validation and intercomparison of the monthly dSEC product is carried out in two stages. First, the yearly trends in the dSEC product are validated against independent measurements from NASA's OIB and ICESat-2 ALT15 data product. Second, we performed an intercomparison of seasonal amplitudes with in situ observations from AWS and elevation change estimates from the altimetry-based SERAC time series.

4.1.1 Validation of trend

To validate the long-term trend of the dSEC product, we compare our dSEC estimates against ICESat-2 ATL15 5 km gridded surface elevation change data (regridded by averaging from the 1 km data product to align with the spatial resolution of the

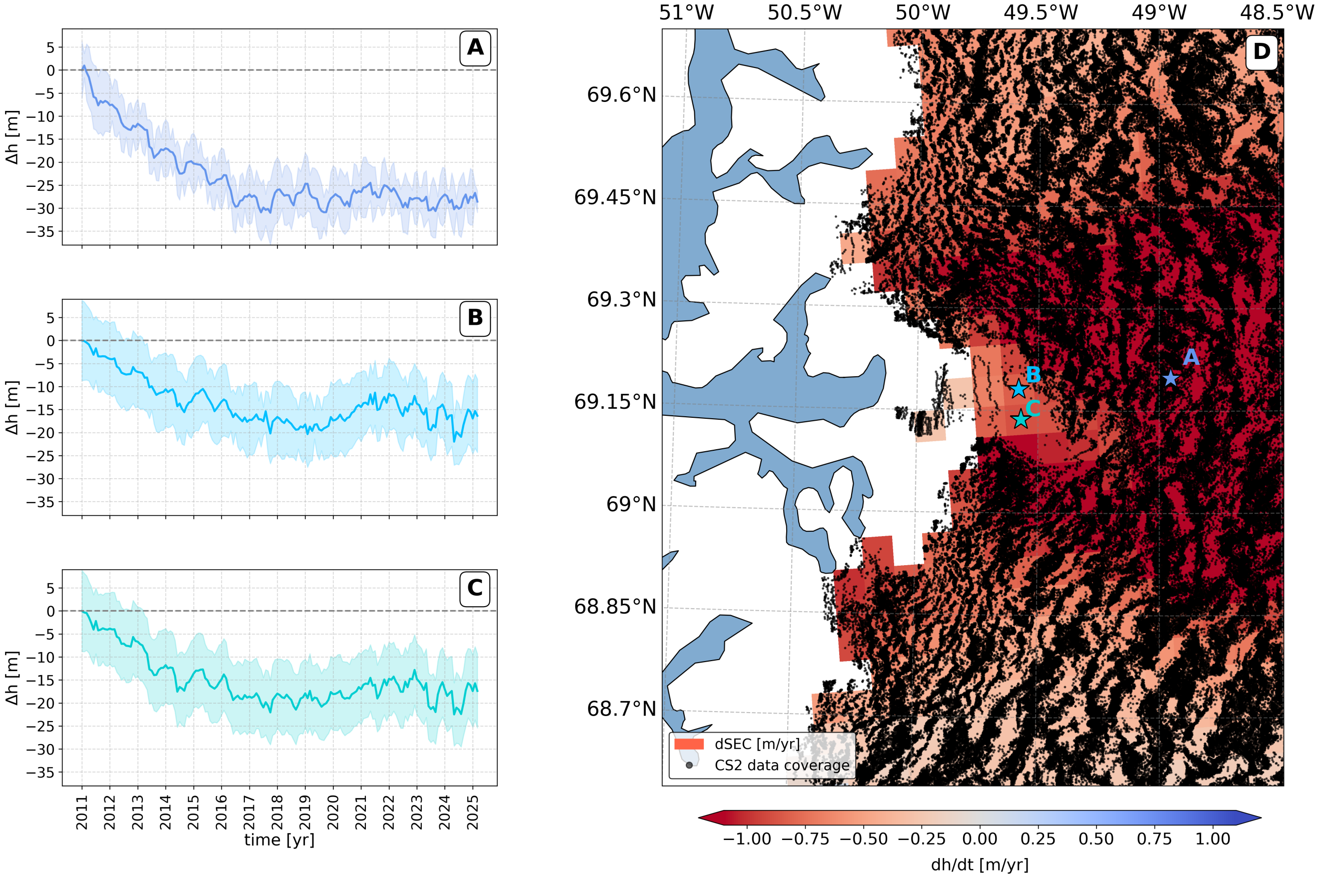

Figure 3. dSEC on Sermeq Kujalleq. Panels **A-C** show time series of dSEC for three selected grid cells (stars), with shaded envelopes indicating model uncertainty. Panel **D** shows the spatial distribution of CryoSat-2 measurements (black dots) and the corresponding dSEC dh/dt map for 2011-2025.

250 dSEC data product) and OIB airborne altimetry measurements. These independent datasets provide complementary spatial and temporal perspectives, allowing for a robust assessment of the performance of our satellite-derived dSEC product. The validation is conducted across multiple time periods, enabling us to investigate consistency and potential biases over time. We analyze both the original (raw) and post-processed (smoothed) versions of the dSEC product to assess the impact of the applied noise-reduction techniques on the agreement with reference datasets.

255 To evaluate the overall agreement between the dSEC product and ICESat-2 ATL15, we first considered that the ATL15 product is provided at 1 km resolution, which we regrid by averaging to a common 5 km grid to match the resolution of our CryoSat-2 dSEC grids. To ensure temporal consistency, we choose the timesteps in our dSEC so that they align with the timesteps of the ICESat-2 ALT15 product. Then we compared the distribution of elevation change differences (dSEC minus ICESat-2 ATL15) for both the raw and smoothed versions (meaning before and after the post-processing step) of the dSEC

https://doi.org/10.5194/egusphere-2025-5015
Preprint. Discussion started: 23 December 2025

dataset (Figure 4). The smoothed dSEC product displays a narrower distribution of differences than the raw version, reducing the standard deviation (STD) from 0.96 to 0.54 m/yr and the median absolute difference (MAD) from 0.24 to 0.1 m/yr. On the Figure 4 the STD of the raw versus smoothed model output was reduced by approximately 44% , and the MAD by around 56% , while the mean difference remained unchanged at 0.11 m/yr. The median differences are close to zero in both cases (-0.01 m/yr for raw and -0.02 m/yr for smoothed), suggesting minimal systematic bias. Across all selected annual periods (Table 2). These results demonstrate that the applied spatio-temporal smoothing effectively reduces high-frequency noise while preserving the underlying elevation change signal.

Table 2. Summary statistics of the difference between dSEC and ICESat-2 ATL15 (dSEC – ATL15) for selected annual periods. Each period includes results for both original (Raw) and post-processed (Smoothed) dSEC products. All values are in m/yr. The final column shows the percentage reduction in standard deviation (STD) after smoothing.

Time Period	Version	Mean	Median	MAD	STD	STD Reduction (%)
Oct 2019 – Oct 2020	Raw	0.16	-0.02	0.25	1.14	–
	Smoothed	0.13	-0.02	0.10	0.63	44.7
Jan 2020 – Dec 2020	Raw	0.21	0.03	0.22	0.97	–
	Smoothed	0.18	0.03	0.10	0.56	42.3
Apr 2020 – Apr 2021	Raw	0.16	0.03	0.22	0.98	–
	Smoothed	0.19	0.03	0.10	0.57	41.8
Jul 2020 – Jul 2021	Raw	0.15	0.07	0.21	1.01	–
	Smoothed	0.12	0.01	0.09	0.54	46.5

To further assess the accuracy of the satellite-derived dSEC estimates, we also validate the data set against multiple campaigns of OIB airborne altimetry data. Figure 5 in Panel A shows a point-by-point comparison between OIB and dSEC values for the raw and smoothed dSEC data set, respectively. After smoothing, the product aligns more closely with the OIB measurements. The smoothing reduces large discrepancies, resulting in a distribution that aligns more closely with the 1:1 line. This improvement is also visible from panel B, where the histogram of the differences in elevation change reveals a narrower distribution for the smoothed data: the STD of the difference between dSEC and OIB SEC is reduced by 50% from 0.78 m/yr in the raw product to 0.37 m/yr after smoothing. Panel C maps the spatial distribution of dSEC–OIB differences across the GrIS, illustrating that the largest residuals are predominantly located around the Sermeq Kujalleq Ice Stream.

The overall results confirm that the spatio-temporal filtering applied to the satellite elevation time series ensures an enhanced agreement with independent airborne validation data, particularly by reducing noise.

4.1.2 Validation of seasonal amplitude using AWS and SERAC data

We evaluate the seasonal amplitude of the dSEC product at three sites (Table 1) using AWS-derived daily relative surface height (Fausto et al., 2021; Vandecrux et al., 2024) and SERAC-FDM fusion (Csatho et al., 2014; Shekhar et al., 2021). By comparing the amplitude of the melt-season signal in our satellite-derived dSEC data with that from AWS time series, we are

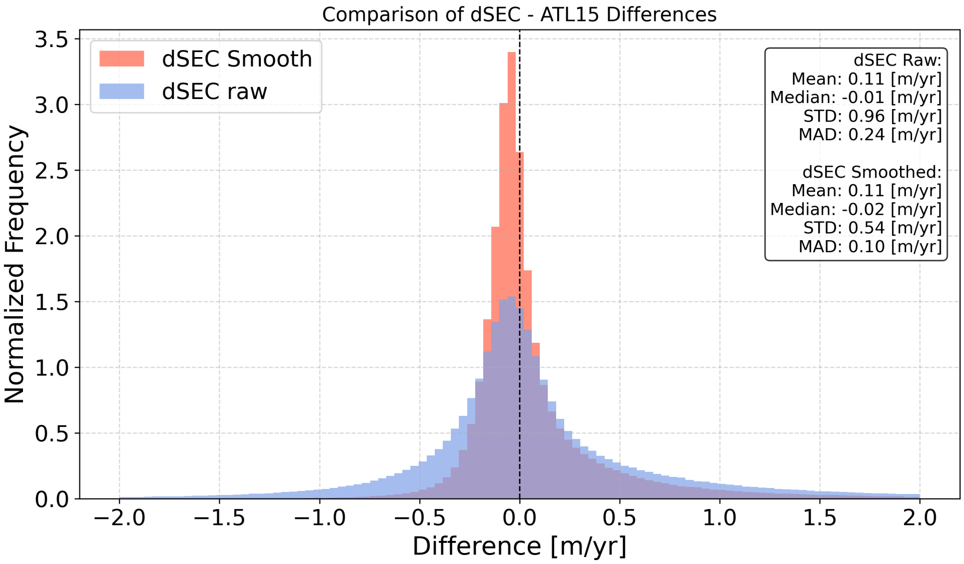

Figure 4. Histogram comparing the differences between the dSEC product (raw and smoothed) with the ICESat-2 ATL15 data over the GrIS.

able to assess the consistency of the dSEC product against independent measurements. The dSEC and SERAC time series are shown in the upper panels of Figure 6.

To assess short-term variability, we compute the average seasonal cycles for these three locations from the linearly detrended time series. The mean seasonal cycles are constructed from the common time period between the dSEC, AWS, and altimetry based SERAC covering the period from 2011 to 2024. These mean seasonal cycles are shown in the lower panels of Figure 6. Across sites, dSEC generally reproduces the phase of seasonal variability observed in both SERAC and AWS, and the amplitude differences between sites are evident. For example, KAN_M shows a pronounced seasonal cycle in all three datasets.

We further quantify the temporal agreement between the three data sets during the period 2011–2024 (the overlap between CryoSat-2 and SERAC) by computing Pearson correlation coefficients between linearly interpolated, detrended dSEC time series and those from AWS and SERAC (Figure 7, and Table 3). The Pearson's correlation coefficient between dSEC and AWS-derived SEC range from 0.58 at JAR to 0.75 at KAN_M. At KAN_M, for example, dSEC correlates moderately with SERAC ($r = 0.75$) and with AWS ($r = 0.75$), suggesting that dSEC captures the temporal variability observed in both records.

5 Discussion

Our results illustrate how our data-driven 3D-ECM framework can advance the monitoring of ice-sheet surface elevation from satellite radar altimetry. By integrating radar altimetry observations with a spatio-temporal statistical model, we obtain continuous, monthly estimates of dSEC over the Greenland Ice Sheet, including regions where satellite sampling is sparse or

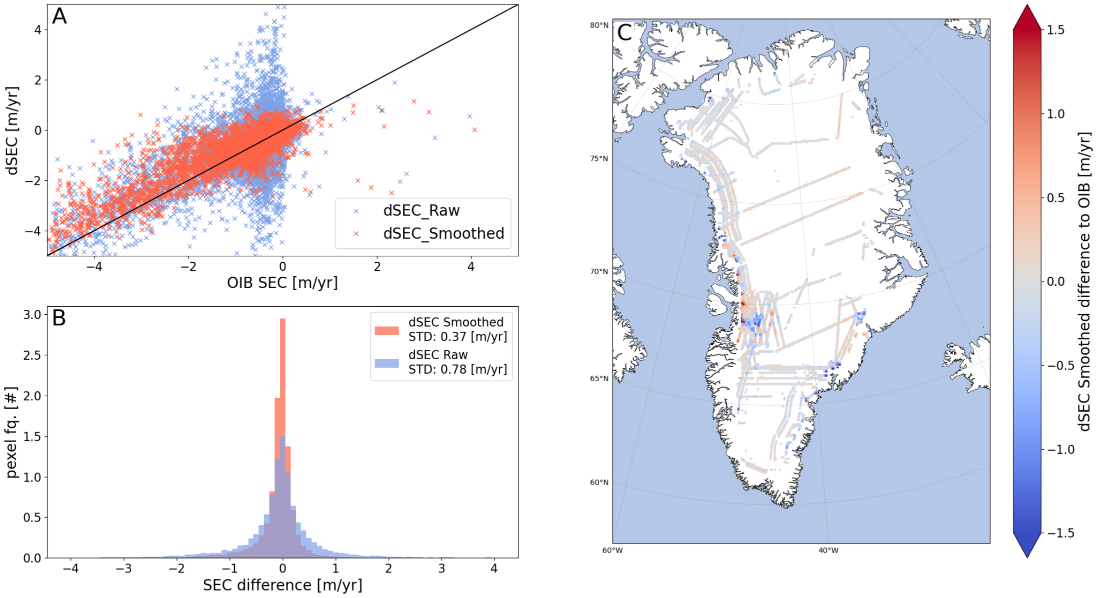

Figure 5. Comparison of CryoSat-2-derived dSEC with OIB airborne altimetry data. **(A)** Scatterplot comparing both the raw (blue) and spatially smoothed (red) dSEC data to OIB SEC values. The 1:1 line is shown in black. **(B)** Histogram of the elevation change differences (dSEC – OIB) for raw (blue) and smoothed (red) data. **(C)** Spatial distribution of the difference between smoothed dSEC and OIB SEC, colored by magnitude of difference (in m/yr).

Table 3. Pearson correlation coefficients (r) between linearly detrended time series from the dSEC product, SERAC and AWS at each station. Correlations are computed over 2011–2024 after linear detrending and interpolation to a common temporal grid.

SERAC station_id	**AWS station_name**	$r_{\text{dSEC vs AWS}}$	$r_{\text{dSEC vs SERAC}}$	$r_{\text{AWS vs SERAC}}$
6002099	JAR	0.584	0.760	0.828
28000270	KPC_U	0.725	0.722	0.926
3001210	KAN_M	0.752	0.744	0.640

irregular. The use of a GMRF to capture spatial dependence, coupled with an autoregressive temporal component, allows the model to isolate meaningful elevation signals while reducing noise.

This capability has important implications for interpreting both seasonal variability and interannual trends in ice sheet surface elevation change. It also highlights the potential to unify data from different altimetry missions and sensor types. Although here we focused on CryoSat-2, the same framework could be applied to past and future radar altimeters, enabling more consistent long-term monitoring across satellite generations.

https://doi.org/10.5194/egusphere-2025-5015
Preprint. Discussion started: 23 December 2025

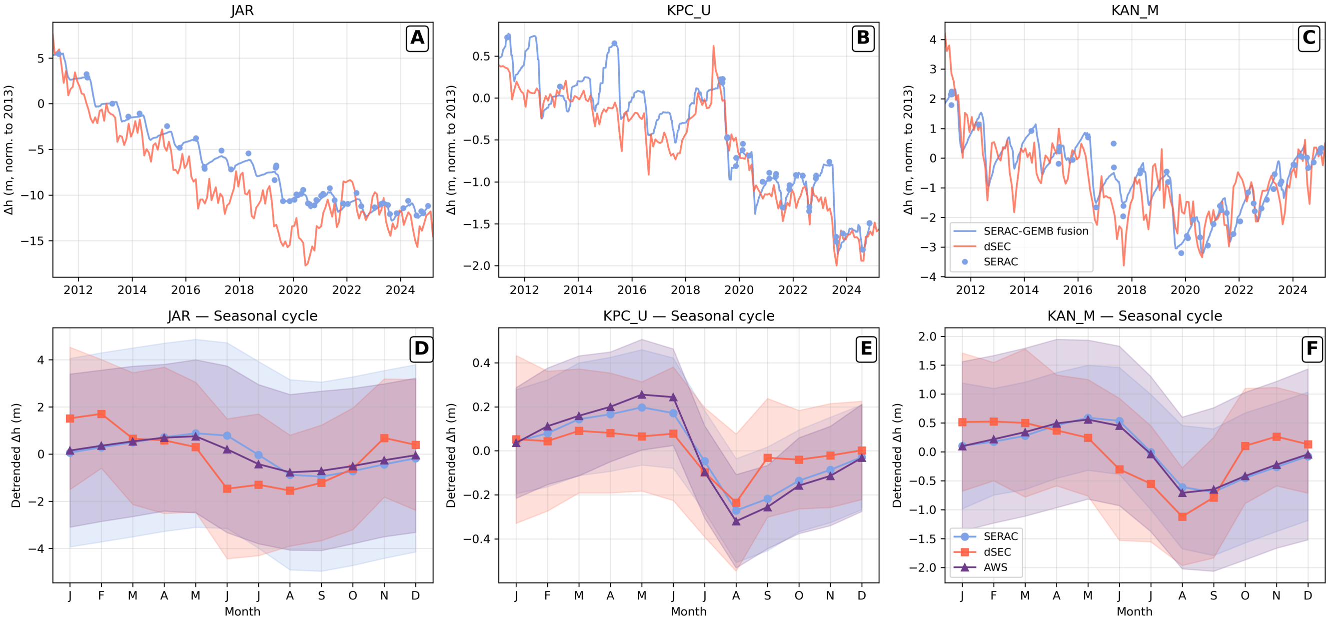

Figure 6. (A–C):Elevation change at three AWS validation sites (JAR, KPC_U, KAN_M). Time series of elevation change from SERAC (blue dots), dSEC (orange), and GEMB (blue), aligned to zero at the start of the CryoSat-2 period (2011) for direct comparison. **(D–F)**: Average seasonal cycles of detrended elevation change for the same stations, based on dSEC (orange), AWS (purple), and SERAC (blue) data, with shaded envelopes indicating $\pm 1\sigma$ statistical variability within each calendar month. Note the different scale on the y-axis. The locations of the AWS stations are shown in Figure 1.

Uncertainty patterns in the dSEC product highlight the dependence of model performance on data density. Figure 3 shows how the uncertainty estimates of the dSEC product are higher in grid cells B (7.1 m ± 1.3 m) and C (7.6 m ± 0.34 m), located within the CryoSat-2 data gap, compared to A (4.8 ± 1.6 m), which is situated in an area with a higher data density. Here, the first value denotes the average uncertainty across the time series, while the ± value represents the temporal variability (standard deviation) of the uncertainty estimate. As expected, model uncertainty increases with distance to available data points; nevertheless, the 3D-ECM reconstructs coherent temporal patterns even in poorly sampled regions. For example, cells B and C capture a pronounced thinning from 2011–2016, consistent with previous studies (Khazendar et al., 2019; Joughin et al., 2020; Hansen et al., 2021), followed by reduced thinning, and reproduce the surface build-up observed between 2019 and 2021 in the trough of the Sermeq Kujalleq Ice Stream (Hansen et al., 2021), despite lying within an almost persistent data gap.

The monthly dSEC product is based on satellite radar altimetry and inherits its sensitivity to changes in surface scattering properties, i.e., the way the radar signal interacts with the surface before it is reflected to the satellite. For instance, an increase in surface roughness will broaden and flatten the returned signal (the waveform), making the identification of the surface reflection more difficult in that waveform (Ridley et al., 1988; Rémy et al., 2009; Ricker et al., 2014). Over polar snow and firn (cold, dry conditions), CryoSat-2's Ku-band (13.6 GHz) radar typically penetrates up to about 1–2 m (Armitage et al.,

https://doi.org/10.5194/egusphere-2025-5015
Preprint. Discussion started: 23 December 2025

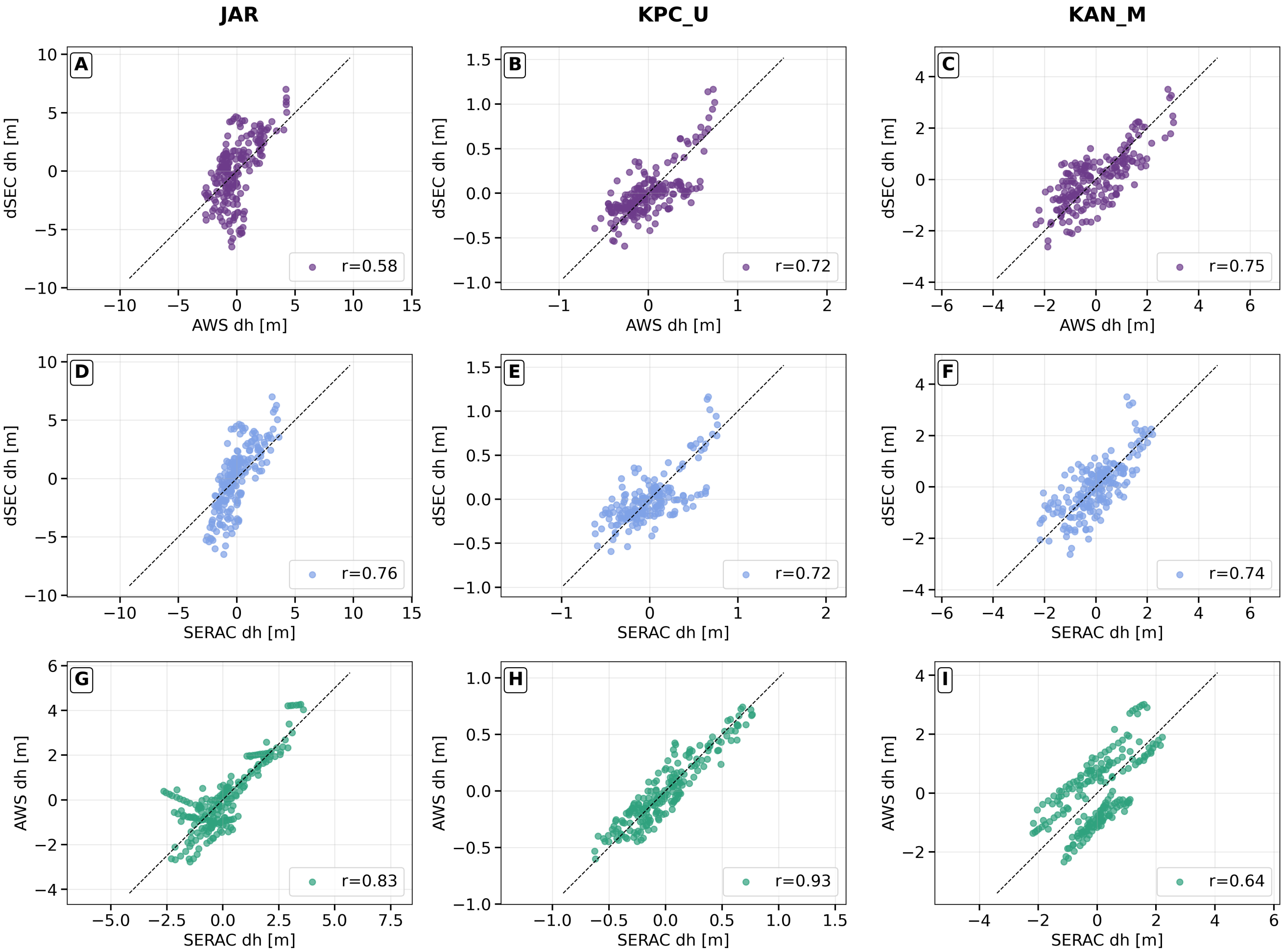

Figure 7. Correlation plots between detrended time series of elevation change. **(A–C)**: dSEC versus AWS for the three validation sites JAR, KPC_U, and KAN_M. **(D–F)**: dSEC versus SERAC for the same sites. **(G–I)**: AWS versus SERAC. Each panel shows the 1:1 line (dashed) and the Pearson correlation coefficient (r).

2014). Variations in volume scattering within that depth range (changes of snow density or grain size) can affect the returned waveform and distort surface elevation estimates (Aublanc et al., 2021; Fredensborg et al., 2024). Likewise, the appearance of an ice layer within that penetration depth may cause a waveform peak at that horizon, which is then interpreted as the surface (Nilsson et al., 2016). Such effects introduce elevation biases that cannot be fully eliminated by statistical smoothing. Consequently, interpretation of dSEC trends must consider changing surface conditions, particularly in regions experiencing melt, refreezing, or firn densification.

Independent validation against ICESat-2 ATL15 and OIB confirms the 3D-ECM method's effectiveness. As shown in the validation analysis, the smoothed dSEC product consistently exhibits reduced spread and lower median absolute deviation compared to the raw product, with annual standard deviations decreased by 40–45 %. These improvements demonstrate that postprocessing of the 3D-ECM effectively suppresses outliers and measurement noise while preserving the underlying signal.

Station-specific comparisons with AWS records and the altimetry-based SERAC product further illustrate how local glaciological conditions affect dSEC interpretation. At JAR (close to Sermeq Kujalleq), dSEC correlates moderately with AWS (r = 0.58) and more strongly with SERAC (r = 0.76). The weaker agreement with AWS likely reflects dynamic ice-thickness changes that are not captured by surface instruments. In contrast, at KPC_U located on an ice lobe north of the Northeast Greenland Ice Stream where seasonal dynamics are minimal—dSEC, AWS, and SERAC show strong agreement (all r > 0.72; AWS–SERAC r = 0.92). KAN_M, in the southwest percolation zone, exhibits high correlation between dSEC and both AWS and SERAC but a lower correlation between AWS and SERAC themselves, consistent with the complex interplay of firn compaction, meltwater infiltration, retention, and refreezing in this region. Notably, both dSEC and SERAC record a shift toward more positive trends around 2020 at KAN_M (Figure 6), suggesting that both datasets capture the same seasonal evolution despite these challenging surface processes.

Taken together, these comparisons indicate that dSEC generally agrees well with both the AWS records and the altimetry-based SERAC product, underscoring the ability of the 3D-ECM framework to extract physically meaningful elevation change signals that are consistent with in situ observations and the altimetry/model-based SERAC. However, these examples also emphasize that while the 3D-ECM framework successfully extracts coherent elevation change patterns, interpretation at the local scale must account for the diverse physical processes that govern different climatic and glaciological regimes across Greenland.

Integration of 3D-ECMs with radar satellite data reveals patterns and anomalies that may remain undetected with sparser observations. Beyond improving the monitoring of the GrIS in great detail, such integration provides valuable input for climate model development. A central novelty of our study lies in the flexibility of the 3D-ECM framework, which is applicable across multiple satellite missions and enables the production of continuous, gap-filled SEC time series at varying spatial and temporal scales. Importantly, the framework is entirely data-driven: seasonal signals emerge directly from observations rather than by an applied season model, in contrast to studies such as Sørensen et al. (2018) and Khan et al. (2025). A potential development for future enhancement of the spatial resolution of the dSEC product is the use of swath-processed CryoSat-2 data (Gray et al., 2013; Gourmelen et al., 2018; Andersen et al., 2021) instead of the Level-2 POCA dataset, due to the higher data density of the swath-processed CryoSat-2 data.

6 Conclusions

We have derived monthly surface elevation change (dSEC) across the Greenland Ice Sheet for the period 2011–2025 from CryoSat-2 radar altimetry. The state-space model combines a Gaussian Markov Random Field for spatial dependencies with an autoregressive temporal process, allowing seasonality, long-term trends, and abrupt changes to emerge directly from the data without prescribing functional forms. The reference surface was taken from ArcticDEM, and analysis was restricted to the ice mask defined by IMBIE (IMBIE Team, 2020).

The resulting dataset captures both broad spatial patterns and local outlet-glacier variability, while providing consistent point-based time series across the ice sheet. Independent validation confirms the robustness of the approach as comparisons with ICESat-2 ATL15 and NASA Operation IceBridge show strong agreement in long-term trends, with spatio-temporal smoothing reducing spread while maintaining minimal bias. Seasonal amplitudes from AWS and SERAC time series also align closely with the linearly detrended dSEC product, demonstrating that the method resolves both interannual and seasonal variability.

Beyond the Greenland application, the modeling framework is directly transferable to other altimetry missions and multi-sensor combinations. Its scalability and statistical rigor enable consistent, long-term monitoring of polar ice sheets and provide a pathway for integrating upcoming missions such as CRISTAL into multi-decadal elevation-change records.

In summary, the presented dSEC dataset delivers monthly, high-resolution, and uncertainty-quantified estimates of surface elevation change across the Greenland ice sheet. The approach enhances the temporal resolution of radar altimetry products, supports improved assessments of ice-sheet mass balance and dynamics, and may establish the foundation for continuous, multi-mission monitoring of the cryosphere.

Data availability.

The dSEC dataset described in this paper provides gridded estimates of monthly elevation change across the Greenland Ice Sheet from January 2011 to March 2025. The full dataset is publicly available through the Technical University of Denmark (DTU) Data repository and can be accessed via the following link: https://figshare.com/s/795f8793cd8bcd870a13?file=56058854. The data are provided in NetCDF format and are compatible with common geospatial tools such as QGIS, allowing for straightforward visualization and analysis. The repository includes the gridded, CF-compliant dSEC data, associated metadata, and documentation to support data use and reproducibility of results. The PROMICE and GC-Net AWS dataset, including the multi-sensor relative surface heights, is available at https://doi.org/10.22008/FK2/IW73UU (How et al., 2022). The SERAC surface elevation change time series, SERAC-GEMB fusion at 10-day resolution, and code are available at https://github.com/hui-97/SERAC-FDM-fusion.git. The CryoSat-2 level2 Baseline E data is available at for download at the ESA FTP site: ftp://science-pds.cryosat.esa.int. The ICESat-2 ATl15 gridded data is available at the NSIDC webpage: https://nsidc.org/data/
The operation icebridge data is available at the NSIDC webpage:https://nsidc.org/data/idhdt4/versions/1

Appendix A: Map of Model Uncertainty

Figure A1 shows the spatial distribution of model uncertainty (posterior standard deviation) for the monthly dSEC product. These uncertainties are obtained directly from the RTMB `sdreport()` output, which provides the marginal posterior standard deviation of the latent spatio-temporal field at each grid cell and each time step.

Higher uncertainties occur in regions with sparse CryoSat-2 coverage (e.g., fast-flowing outlet glaciers with persistent data gaps), while the interior of the ice sheet shows substantially lower uncertainty due to denser and more stable altimetric sampling. This spatial pattern is consistent with expectations from the GMRF structure and the temporal AR(1) evolution used in the 3D-ECM. In addition, tile boundaries are visible in the map; these arise because the model is run in overlapping spatial tiles for computational efficiency, which can introduce subtle differences along tile edges.

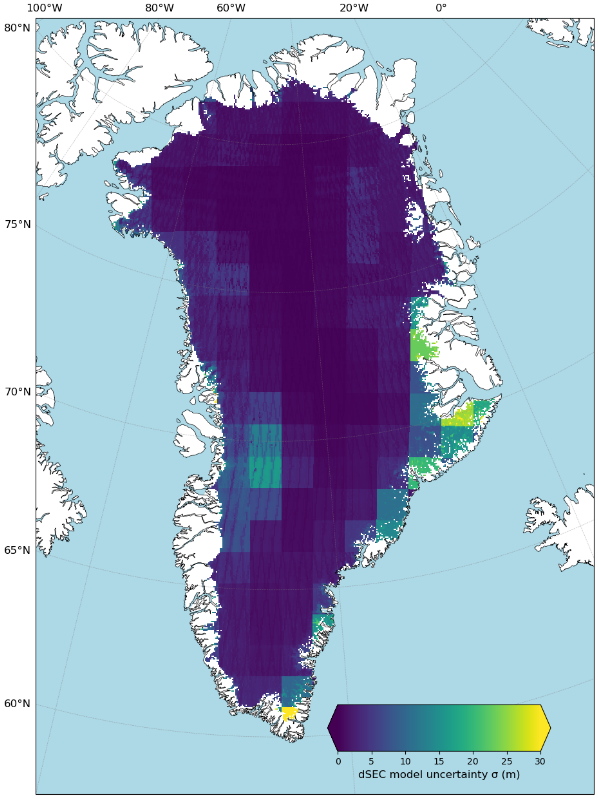

Figure A1. Spatial distribution of the uncertainty of the dSEC model field. Areas with sparse CryoSat–2 observations exhibit higher uncertainty, while interior regions with denser coverage show substantially lower uncertainty.

Spatial distribution of the posterior standard deviation of the dSEC model field. Areas with sparse CryoSat–2 observations exhibit higher uncertainty, while interior regions with denser coverage show substantially lower uncertainty.

Author contributions.

Natalia H. Andersen: Main technical author, set up the state-space model, performed validation, and wrote the manuscript. **Sebastian B. Simonsen**: Part of the analysis board, contributed to the methodology, and provided feedback on the manuscript. **Karina Nielsen**: Set up the model in R and contributed methodological support. **Mai Winstrup**: Contributed to the interpretation of results and scientific discussion. **Baptiste Vandecrux**: Provided AWS validation data, scientific discussion, and provided feedback on the manuscript. **Hui Gao, Bea Csatho, and Anton Schenk**: Contributed SERAC altimetry-based validation data and scientific discussion. **Louise Sandberg Sørensen**: Supervised the work, provided domain expertise, and provided feedback on the manuscript.

Competing interests.

At least one of the (co-)authors is a member of the editorial board of The Cryosphere. The authors also have no other competing interests to declare.

Acknowledgements. The work presented in this paper has been funded through European Space Agencys (ESA) Climate Change Initiative (ESA CCI+) Greenland Ice Sheet via ESA-ESRIN contract number 4000104815/11/I-NB. The PROMICE and GC-Net programs are supported by Denmark's Ministry of Climate, Energy, and Utilities through the Danish Cooperation for Environment in the Arctic. We thank Ivan Parmuzin for the technical support in processing the SERAC surface elevation change time series. We thank Nicole Schlegel for the GEMB model outputs.

References

Adhikari, S., Milne, G. A., Caron, L., Khan, S. A., Kjeldsen, K. K., Nilsson, J., et al.: Decadal to Centennial Timescale Mantle Viscosity Inferred From Modern Crustal Uplift Rates in Greenland, Geophys. Res. Lett., 48(19), e2021GL094040, https://doi.org/10.1029/2021GL094040, 2021.

Ahlstrøm, A. P., PROMICE project team. A new programme for monitoring the mass loss of the Greenland ice sheet. GEUS Bulletin, 15, 61-64. https://doi.org/10.34194/geusb.v15.5045, 2008.

Andersen, N. H., Simonsen, S. B., Winstrup, M., Nilsson, J., Sørensen, L. S. Regional assessments of surface ice elevations from swath-processed SARin data from CryoSat-2. *Remote Sensing*, 13(2213), 1–15, https://doi.org/10.3390/rs13112213 , 2021.

T. W. K. Armitage and M. W. J. Davidson, "Using the Interferometric Capabilities of the ESA CryoSat-2 Mission to Improve the Accuracy of Sea Ice Freeboard Retrievals," in IEEE Transactions on Geoscience and Remote Sensing, vol. 52, no. 1, pp. 529-536, Jan. 2014, doi: 10.1109/TGRS.2013.2242082. , 2014.

Aublanc, J., Thibaut, P., Guillot, A., Boy, F., Picot, N. Ice Sheet Topography from a New CryoSat-2 SARIn Processing Chain, and Assessment by Comparison to ICESat-2 over Antarctica. Remote Sensing, 13(22), 4508. https://doi.org/10.3390/rs13224508 , 2021.

Bamber, J., & Riva, R. The sea level fingerprint of recent ice mass fluxes. *The Cryosphere*, 4, 621–627. https://doi.org/10.5194/tc-4-621-2010 ,2010.

Bevan, S. L., Luckman, A., Khan, S. A., and Murray, T. Seasonal dynamic thinning at Helheim Glacier. *Earth and Planetary Science Letters*, 415, 47–53, https://doi.org/10.1016/j.epsl.2015.01.031, 2015.

Bouzinac, C. *CryoSat-2 Product Handbook* (Baseline-E 1.0 — Draft C, Doc ID: C2-LI-ACS-ESL-5319. European Space Agency. https://earth.esa.int/eogateway/documents/20142/0/CryoSat-Product-Handbook-Baseline-E-draft.pdf , 2019.

Box, J. E., Hubbard, A., Bahr, D. B., Colgan, W. T., Fettweis, X., Mankoff, K. D., Wehrlé, A., Noël, B., van den Broeke, M. R., Wouters, B., Bjørk, A. A., and Fausto, R. S. Greenland ice sheet climate disequilibrium and committed sea-level rise. *Nature Climate Change*, 12, 808–813. https://doi.org/10.1038/s41558-022-01441-2 , 2022.

Chylek, P., Folland, C. K., Klett, J. D., Wang, M., Hengartner, N., Lesins, G., & Dubey, M. K. Annual mean Arctic amplification 1970–2020: Observed and simulated by CMIP6 climate models. *Geophysical Research Letters*, 49, e2022GL099371. https://doi.org/10.1029/2022GL099371 , 2022.

Csatho, B. M., Schenk, A. F., van der Veen, C. J., Babonis, G., Duncan, K., Rezvanbehbahani, S., et al.: Laser altimetry reveals complex pattern of Greenland Ice Sheet dynamics, Proc. Natl. Acad. Sci. USA, 111(52), 18478–18483, https://doi.org/10.1073/pnas.1411680112, 2014.

Fausto, R. S., van As, D., Mankoff, K. D., Vandecrux, B., Citterio, M., Ahlstrøm, A. P., Andersen, S. B., Colgan, W., Karlsson, N. B., Kjeldsen, K. K., Korsgaard, N. J., Larsen, S. H., Nielsen, S., Pedersen, A.Ø., Shields, C. L., Solgaard, A. M., and Box, J. E. Programme for Monitoring of the Greenland Ice Sheet (PROMICE) automatic weather station data. *Earth System Science Data*, **13**(8), 3819–3845. doi:10.5194/essd-13-3819-2021 , 2021.

Greenland and Antarctica Ice Sheet Mass Changes and Effects on Global Sea Level. In A. Cazenave, N. Champollion, F. Paul, & J. Benveniste (Eds.), *Integrative Study of the Mean Sea Level and Its Components* (Space Sciences Series of ISSI, vol. 58, pp. 91–106). Springer, Cham. https://doi.org/10.1007/978-3-319-56490-6_5 , 2017.

Fredensborg Hansen, R. M., Skourup, H., Rinne, E., Jutila, A., Lawrence, I. R., Shepherd, A., Høyland, K. V., Li, J., Rodriguez-Morales, F., Simonsen, S. B., Wilkinson, J., Veyssiere, G., Yi, D., Forsberg, R., and Casal, T. G. D.: Exploring microwave penetration into snow on Antarctic summer sea ice along CryoSat-2 and ICESat-2 (CRYO2ICE) orbit from multi-frequency air- and spaceborne altimetry, EGUsphere [preprint], https://doi.org/10.5194/egusphere-2024-2854, 2024.

Gallagher, N. B. Savitzky-Golay smoothing and differentiation filter. Control System Engineering. https://doi.org/10.13140/RG.2.2.20339.50725 , 2020.

Gardner, A. S., Moholdt, G., Scambos, T., et al. A reconciled estimate of glacier contributions to sea-level rise: 2003 to 2009. *Science*, 340(6134), 852-857 https://doi.org/10.1126/science.1234532 , 2013.

Gardner, A. S., Schlegel, N.-J., and Larour, E.: Glacier Energy and Mass Balance (GEMB): a model of firn processes for cryosphere research, Geosci. Model Dev., 16(8), 2277–2302, https://doi.org/10.5194/gmd-16-2277-2023, 2023.

Gourmelen, N., Escorihuela, M., Shepherd, A., et al. CryoSat-2 swath interferometric altimetry for mapping ice elevation and elevation change. *Advances in Space Research*, 62(6), 1226-1242. https://doi.org/10.1016/j.asr.2017.11.014, 2018.

Gray, L., Burgess, D., Copland, L., et al. Interferometric swath processing of Cryosat data for glacial ice topography. *Cryosphere*, 7, 1857–1867, https://doi.org/10.5194/tc-7-1857-2013 , 2013.

Hansen, K., Truffer, M., Aschwanden, A., Mankoff, K., Bevis, M., Humbert, A., van den Broeke, M. R., Noël, B., Bjørk, A., Colgan, W., Kjær, K. H., *et al.* Estimating ice discharge at Greenland's three largest outlet glaciers using local bedrock uplift. *Geophysical Research Letters*, 48(13), e2021GL094252, https://doi.org/10.1029/2021GL094252, 2021.

How, P.; Lund, M.C.; Ahlstrøm, A.P.; Andersen, S.B.; Box, J.E.; Citterio, M.; Colgan, W.T.; Fausto, R.S.; Karlsson, N.B.; Jakobsen, J.; Jakobsgaard, H.T.; Larsen, S.H.; Mankoff, K.D.; Nielsen, R.B.; Rutishauser, A.; Shield, C.L.; Solgaard, A.M.; Stevens, I.T.; van As, D.; Vandecrux, B.; Abermann, J.; Bjørk, A.A.; Langley, K.; Lea, J.; Prinz, R., "PROMICE and GC-Net automated weather station data in Greenland", https://doi.org/10.22008/FK2/IW73UU, GEUS Dataverse, V27, 2022.

The IMBIE Team. Mass balance of the Greenland Ice Sheet from 1992 to 2018. *Nature*, 579, 233–239, https://doi.org/10.1038/s41586-019-1855-2 , 2020.

Joughin, I., Shean, D. E., Smith, B. E., and Floricioiu, D. A decade of variability on Jakobshavn Isbræ: Ocean temperatures pace speed through influence on mélange rigidity. *The Cryosphere*, 14(1), 211–227 , https://doi.org/10.5194/tc-14-211-2020 , 2020.

Kehrl, L. M., Joughin, I., Shean, D. E., Floricioiu, D., and Krieger, L. Seasonal and interannual variabilities in terminus position, glacier velocity, and surface elevation at Helheim and Kangerlussuaq Glaciers from 2008 to 2016. *Journal of Geophysical Research: Earth Surface*, 122(8), 1635–1652, https://doi.org/10.1002/2016JF004133 , 2017.

Khan, S. A., Mernild, S. H., Kjeldsen, K. K. Accelerating ice loss from peripheral glaciers in North Greenland. *Geophysical Research Letters*, 49(12), e2022GL098915, https://doi.org/10.1029/2022GL098915 , 2022.

Khan, S. A., Seroussi, H., Morlighem, M., Colgan, W., Helm, V., Cheng, G., Berg, D., Barletta, V. R., Larsen, N. K., Kochtitzky, W., van den Broeke, M., Kjær, K. H., Aschwanden, A., Noël, B., Box, J. E., MacGregor, J. A., Fausto, R. S., Mankoff, K. D., Howat, I. M., Oniszk, K., Fahrner, D., Løkkegaard, A., Lippert, E. Y. H., Bråtner, A., & Hassan, J. Smoothed monthly Greenland ice sheet elevation changes during 2003–2023. *Earth System Science Data*, 17, 3047–3071. https://doi.org/10.5194/essd-17-3047-2025 , 2025.

Khazendar, A., Fenty, I. G., Carroll, D., Gardner, A., Lee, C. M., Fukumori, I., *et al.* Interruption of two decades of Jakobshavn Isbræ acceleration and thinning as regional ocean cools. *Nature Geoscience*, 12(4), 277–283, https://doi.org/10.1038/s41561-019-0329-3, 2019

Kristensen, K., Nielsen, A., Berg, C. W., Skaug, H., Bell, B. M. TMB: Automatic Differentiation and Laplace Approximation. *Journal of Statistical Software*, 70(5), 1–21, https://doi.org/10.18637/jss.v070.i05 , 2016.

Lai, Y.-R., and Wang, L. Monthly surface elevation changes of the Greenland Ice Sheet from ICESat-1, CryoSat-2, and ICESat-2 altimetry missions. *IEEE Geoscience and Remote Sensing Letters*, 19, 1–5, Art. no. 2000305 , https://doi.org/10.1109/LGRS.2021.3058956 , 2022.

Liu, L., Khan, S. A., van Dam, T., Ma, J. H. Y., and Bevis, M. Annual variations in GPS-measured vertical displacements near Upernavik Isstrøm (Greenland) and contributions from surface mass loading. *Journal of Geophysical Research: Solid Earth*, 122(1), 718–734, https://doi.org/10.1002/2016JB013494 , 2017.

Løkkegaard, A., Colgan, W., Hansen, K., et al. Ice acceleration and rotation in the Greenland Ice Sheet interior in recent decades. *Commun Earth Environ*, 5, 211, https://doi.org/10.1038/s43247-024-01322-w , 2024.

MacGregor, J. A., Boisvert, L. N., Medley, B., Petty, A. A., Harbeck, J. P., Bell, R. E., et al.: The Scientific Legacy of NASA's Operation IceBridge, Rev. Geophys., 59(2), e2020RG000712, https://doi.org/10.1029/2020RG000712, 2021.

Markus, T., Neumann, T., Martino, A., Abdalati, W., Brunt, K., Csatho, B., et al.: The Ice, Cloud, and land Elevation Satellite-2 (ICESat-2): Science requirements, concept, and implementation, Remote Sens. Environ., 190, 260–273, https://doi.org/10.1016/j.rse.2016.12.029, 2017.

Milne, G. A., Latychev, K., Schaeffer, A., Crowley, J. W., Lecavalier, B. S., and Audette, A.: The influence of lateral Earth structure on glacial isostatic adjustment in Greenland, Geophys. J. Int., 214(2), 1252–1266, https://doi.org/10.1093/gji/ggy189, 2018.

Moon, T., Sutherland, D. A., Carroll, D., et al. Subsurface iceberg melt key to Greenland fjord freshwater budget. *Nature Geoscience*, 11, 49–54 , https://doi.org/10.1038/s41561-017-0018-z , 2018.

Mouginot, J., Rignot, E., Bjørk, A. A., van den Broeke, M., Millan, R., Morlighem, M., Noël, B., Scheuchl, B., and Wood, M. Forty-six years of Greenland Ice Sheet mass balance from 1972 to 2018. *Proceedings of the National Academy of Sciences*, 116(19), 9239–9244 , https://doi.org/10.1073/pnas.1904242116 , 2019.

Nielsen, K., Zakharova, E., Tarpanelli, A., Andersen, O. B., Benveniste, J. River levels from multi mission altimetry, a statistical approach. *Remote Sensing of Environment*, **270**, 112876, ISSN 0034-4257. https://doi.org/10.1016/j.rse.2021.112876. https://www.sciencedirect.com/science/article/pii/S0034425721005964 , 2022.

Nilsson, J., Gardner, A., Sandberg Sørensen, L., and Forsberg, R.: Improved retrieval of land ice topography from CryoSat-2 data and its impact for volume-change estimation of the Greenland Ice Sheet, The Cryosphere, 10, 2953–2969, https://doi.org/10.5194/tc-10-2953-2016, 2016.

Nilsson, J. and Gardner, A. S.: Elevation Change of the Greenland Ice Sheet and its Peripheral Glaciers: 1992–2023, Earth Syst. Sci. Data Discuss. [preprint], https://doi.org/10.5194/essd-2024-311, 2024.

Otosaka, I.N., Horwath, M., Mottram, R. et al. Mass Balances of the Antarctic and Greenland Ice Sheets Monitored from Space. *Surv. Geophys.* **44**, 1615–1652, https://doi.org/10.1007/s10712-023-09795-8 , 2023.

Porter, Claire; Howat, Ian; Noh, Myoung-Jon; Husby, Erik; Khuvis, Samuel; Danish, Evan; Tomko, Karen; Gardiner, Judith; Negrete, Adelaide; Yadav, Bidhyananda; Klassen, James; Kelleher, Cole; Cloutier, Michael; Bakker, Jesse; Enos, Jeremy; Arnold, Galen; Bauer, Greg; Morin, Paul, "ArcticDEM - Mosaics, Version 4.1", Harvard Dataverse, V1 https://doi.org/10.7910/DVN/3VDC4W , 2023.

Rantanen, M., Karpechko, A. Y., Lipponen, A., et al. The Arctic has warmed nearly four times faster than the globe since 1979. *Commun Earth Environ*, 3, 168 , https://doi.org/10.1038/s43247-022-00498-3 , 2023.

Ravinder, N., Shepherd, A., Otosaka, I., Slater, T., Muir, A., and Gilbert, L. Greenland Ice Sheet elevation change from CryoSat-2 and ICESat-2. *Geophysical Research Letters*, 51, e2024GL110822 , https://doi.org/10.1029/2024GL110822 , 2024.

Rémy, F., & Parouty, S. Antarctic Ice Sheet and Radar Altimetry: A Review. *Remote Sensing*, 1(4), 1212–1239. https://doi.org/10.3390/rs1041212 , 2009.

Ricker, R., Hendricks, S., Helm, V., Skourup, H., and Davidson, M.: Sensitivity of CryoSat-2 Arctic sea-ice freeboard and thickness on radar-waveform interpretation, The Cryosphere, 8, 1607–1622, https://doi.org/10.5194/tc-8-1607-2014, 2014.

Ridley, J. K., & Partington, K. C. A model of satellite radar altimeter return from ice sheets. *International Journal of Remote Sensing*, 9(4), 601–624. https://doi.org/10.1080/01431168808954881 , 1988.

Rignot, E., & Mouginot, J. Ice flow in Greenland for the International Polar Year 2008–2009. *The Cryosphere*, 6, 115–123. https://doi.org/10.1029/2012GL051634 , 2012.

Rue, H. and Held, L. Gaussian Markov Random Fields: Theory and Applications. Chapman & Hall/CRC, Monographs on Statistics and Applied Probability, Vol. 104, https://doi.org/10.1201/9780203492024 , 2005.

Schenk, T., Csatho, B., van der Veen, C., and McCormick, D.: Fusion of multi-sensor surface elevation data for improved characterization of rapidly changing outlet glaciers in Greenland, Remote Sens. Environ., 149, 239–251, https://doi.org/10.1016/j.rse.2014.04.005, 2014.

Schenk, T., and Csatho, B.: A New Methodology for Detecting Ice Sheet Surface Elevation Changes From Laser Altimetry Data, IEEE Trans. Geosci. Remote Sens., 50(9), 3302–3316, https://doi.org/10.1109/TGRS.2011.2182357, 2012.

Shekhar, P., Csatho, B., Schenk, T., Roberts, C., and Patra, A. K.: ALPS: A Unified Framework for Modeling Time Series of Land Ice Changes, IEEE Trans. Geosci. Remote Sens., 59(8), 6466–6481, https://doi.org/10.1109/TGRS.2020.3027190, 2021.

Simonsen, S. B., Sørensen, L. S. Implications of changing scattering properties on Greenland ice sheet volume change from CryoSat-2 altimetry. *Remote Sensing of Environment*, 190, 207–216, https://doi.org/10.1016/j.rse.2016.12.012 , 2017.

Simonsen, S. B., Barletta, V. R., Colgan, W. T., Sørensen, L. S. Greenland Ice Sheet mass balance (1992–2020) from calibrated radar altimetry. Geophysical Research Letters, 48, e2020GL091216. https://doi.org/10.1029/2020GL091216 , 2021.

Smith, B., Sutterley, T., Dickinson, S., Jelley, B. P., Felikson, D., Neumann, T. A., Fricker, H. A., Gardner, A. S., Padman, L., Markus, T., Kurtz, N., Bhardwaj, S., Hancock, D. & Lee, J. ATLAS/ICESat-2 L3B Gridded Antarctic and Arctic Land Ice Height Change. (ATL15, Version 2). [Data Set - Date Accessed 04-01-2025]. Boulder, Colorado USA. NASA National Snow and Ice Data Center Distributed Active Archive Center. https://doi.org/10.5067/ATLAS/ATL15.002 , 2022.

Studinger, M. IceBridge ATM L4 Surface Elevation Rate of Change. (IDHDT4, Version 1). [Data Set]. Boulder, Colorado USA. NASA National Snow and Ice Data Center Distributed Active Archive Center. https://doi.org/10.5067/BCW6CI3TXOCY , 2014.

Sweeney, A. J., Fu, Q., Po-Chedley, S., Wang, H., & Wang, M. Internal variability increased Arctic amplification during 1980–2022. *Geophysical Research Letters*, 50, e2023GL106060. https://doi.org/10.1029/2023GL106060 , 2023.

Sørensen, L., Simonsen, S., Forsberg, R., Khvorostovsky, K., Meister, R., Engdahl, M. E. 25 years of elevation changes of the Greenland Ice Sheet from ERS, Envisat, and CryoSat-2 radar altimetry. *Earth and Planetary Science Letters*, 495, 234–241, https://doi.org/10.1016/j.epsl.2018.05.015 , 2018.

Vandecrux, B., Fausto, R. S., Box, J. E., Covi, F., Hock, R., Rennermalm, Å. K., Heilig, A., Abermann, J., van As, D., Bjerre, E., Fettweis, X., Smeets, P. C. J. P., Kuipers Munneke, P., van den Broeke, M. R., Brils, M., Langen, P. L., Mottram, R., and Ahlstrøm, A. P. Recent warming trends of the Greenland ice sheet documented by historical firn and ice temperature observations and machine learning. *The Cryosphere*, 18, 609–631 , https://doi.org/10.5194/tc-18-609-2024 , 2024

Williams, J. J., Gourmelen, N., Nienow, P. Complex multi-decadal ice dynamical change inland of marine-terminating glaciers on the Greenland Ice Sheet. *Journal of Glaciology*, 67(265), 833-846, https://doi.org/10.1017/jog.2021.31, 2021.

Wingham, D.J., Francis, C.R., Baker, S., Bouzinac, C., Brockley, D., Cullen, R., de Chateau-Thierry, P., Laxon, S.W., Mallow, U., Mavrocordatos, C., Phalippou, L., Ratier, G., Rey, L., Rostan, F., Viau, P., and Wallis, D.W. CryoSat: A mission to determine the fluctuations in Earth's land and marine ice fields. *Advances in Space Research*, **37**(4), 841–871. https://doi.org/10.1016/j.asr.2005.07.027 , 2006.

Zhang, B., Wang, Z., An, J., Liu, T., and Geng, H.: A 30-year monthly 5 km gridded surface elevation time series for the Greenland Ice Sheet from multiple satellite radar altimeters, Earth Syst. Sci. Data, 14, 973–988, https://doi.org/10.5194/essd-14-973-2022, 2022.

560 Zwally, H. J., Schutz, B., Abdalati, W., Abshire, J., Bentley, C., Brenner, A., et al.: ICESat's laser measurements of polar ice, atmosphere, ocean, and land, J. Geodyn., 34(3), 405–445, https://doi.org/10.1016/S0264-3707(02)00042-X, 2002.